

# DETERMINING DEBRIS CHARACTERISTICS FROM OBSERVABILITY ANALYSIS OF ARTIFICIAL NEAR-EARTH OBJECTS

A. M. Friedman and C. Frueh

*Purdue University, School of Aeronautics and Astronautics, 701 W. Stadium Avenue, West Lafayette, IN 47907, USA,  
Email: {friedmaa, cfrueh}@purdue.edu*

## ABSTRACT

Observability analysis is a method for determining whether a chosen state can be determined from measurements. The state is typically composed of position and velocity; however, including object characteristics beyond position and velocity can be crucial for precise orbit propagation. For example, solar radiation pressure has a significant impact on the orbit of high area-to-mass ratio objects in geosynchronous orbit. Therefore, determining the time required for solar radiation pressure parameters to become observable is important for understanding debris objects. The focus of this work is the development and implementation of an extended state discrete time-varying observability analysis tool for debris objects. Previous results on incorporating measurement noise into observability analysis are implemented to determine the effect of measurement noise on extended state observability analysis. Ten objects, five low Earth objects and five geosynchronous objects, are simulated for several non-extended and extended state vector cases. The times to become observable are compared for the different extended state vectors and the different measurement noise cases. The impact of using an extended state vector in observability analysis for determining debris object characteristics is discussed.

Keywords: Observability; Extended State; Solar Radiation Pressure.

## 1. INTRODUCTION

As the space debris population continues to grow from the almost 60 years of humankind's exploration of space, so does the concern for satellites and astronauts in orbit around Earth. The current estimate of the number of debris objects in orbit around Earth is over 100 million greater than 1 mm in size [9]. While a majority of the debris objects in orbit around Earth are on the sub-centimeter scale and would not appear to be much of a threat because of their small size, the high orbit energy of objects means that even objects on the millimeter scale have the potential to damage assets in orbit [7]. Even

with the addition of the Space Fence, which will be able to track up to 200,000 objects greater than one centimeter in size, many of the debris objects on orbit will go untracked [11]. Therefore, the ground station resources available for tracking space debris objects will be insufficient to completely track the debris population. With this information, importance should be placed on gaining as much information about space debris from each observation and tracking objects as efficiently as possible.

Observability analysis can be instrumental in improving sensor tasking efficiency and determining more information about active satellites and debris objects. Potential applications of applying observability analysis to the space object problem are sensor tasking, planning of future ground stations, improved estimation methods, and object characterization. This paper will focus on implementation of observability analysis for determining object characteristics.

Previous work on the incorporation of measurement noise into observability analysis reviewed various applications of observability analysis [4, 5]. Extending the state vector in observability analysis has been used in work by Dianetti [3]. In the work by Dianetti, observability analysis is performed to determine when a parameter should be estimated in a consider filter framework. Rather than specifically using observability analysis as a tool for determining when a parameter should be estimated or not, this work looks more generally at extended state observability analysis, its implications, and how adding extra parameters in the analysis can be used for determining object characteristics. Furthermore, the effect of extending the state on the time for a system to become observable is investigated. The paper is organized as follows. First, the observability methods implemented and the dynamical models used are introduced. Next, incorporation of an extended state vector into discrete time observability analysis is given. The paper concludes with numerical results of several extended state cases and conclusions.

## 2. METHODS

In this section the discrete time-varying observability matrix is derived for a linearized system. In addition, the dy-

nomical model including solar radiation pressure (SRP) and the Jacobian of the dynamics with respect to the state vector are defined for several extended state cases. Moreover, the measurement model used in the observability analysis is defined.

## 2.1. Observability Analysis

Previous work on observability analysis was implemented with continuous time-varying methods [4]. The continuous time-varying observability methods were used as a first step to creating a observability tool for determining debris object characteristics. The discrete time-varying observability matrix is used in this work on extended state observability. An advantage of the discrete-time formulation is that it can be applied with observations spaced realistically. However, as a starting point with the discrete-time observability analysis and with the extended state observability, this analysis is applied without restrictions on how observations are spaced.

The system in which these debris objects operate is nonlinear, given by the following equations.

$$\dot{\mathbf{x}}(t_k) = \mathbf{f}(t_k, \mathbf{x}(t_k)), \quad (1)$$

$$\mathbf{y}(t_k) = \mathbf{h}(t_k, \mathbf{x}(t_k)). \quad (2)$$

In Equations 1 and 2,  $t_k$  is the time at each measurement,  $\mathbf{x}(t_k)$  is the state vector,  $\mathbf{y}(t_k)$  is the output or measurements,  $\mathbf{f}(t_k, \mathbf{x}(t_k))$  is a nonlinear function of the dynamics, and  $\mathbf{h}(t_k, \mathbf{x}(t_k))$  is a nonlinear function of the measurements. The state vector in observability analysis typically only contains position and velocity, but this work focuses on extending the state vector to contain further debris object characteristics.

Equations 1 and 2 can be linearized in two ways: with state and measurement variations, as in [1, 8, 15, 16], or with the Jacobian, as in [8]. A linearization using the Jacobian given in Montenbruck [8] is used to determine the state space equations below.

$$\dot{\mathbf{x}}(t_k) = \mathbf{A}(t_k) \mathbf{x}(t_k), \quad (3)$$

$$\mathbf{y}(t_k) = \tilde{\mathbf{H}}(t_k) \mathbf{x}(t_k) + \nu. \quad (4)$$

In Equations 3 and 4,  $\mathbf{A}(t_k)$  contains the linearized dynamics,  $\tilde{\mathbf{H}}(t_k)$  is the linearized measurement matrix, and  $\nu$  is the measurement noise. From the linearized equations above, the discrete-time observability matrix can be determined with the following. The fundamental question of observability is whether or not the initial state  $\mathbf{x}_0$  can be determined from the measurements  $\mathbf{y}(t_k)$ . Since this is a linearized system, the state transition matrix (STM),  $\Phi(t_k, t_0)$ , operates on the states by:

$$\mathbf{x}(t_k) = \Phi(t_k, t_0) \mathbf{x}(t_0), \quad (5)$$

where  $\Phi(t, t_0)$  is numerically determined from the STM differential equation:

$$\dot{\Phi}(t_k, t_0) = \mathbf{A}(t_k) \Phi(t_k, t_0), \quad (6)$$

with  $\Phi(t_0, t_0) = I_{n \times n}$ . Substituting Equation 5 into the measurement equation, the observability matrix is formed with matrix manipulation.

$$\mathbf{y}(t_k) = \tilde{\mathbf{H}}(t_k) \Phi(t_k, t_0) \mathbf{x}(t_0), \quad (7)$$

Letting,

$$\mathbf{H}(t_k) = \tilde{\mathbf{H}}(t_k) \Phi(t_k, t_0), \quad (8)$$

and multiplying both sides on the left by  $\mathbf{H}(t_k)^T$ ,

$$\mathbf{H}(t_k)^T \mathbf{y}(t_k) = \mathbf{H}(t_k)^T \mathbf{H}(t_k) \mathbf{x}(t_0). \quad (9)$$

A system is deemed observable when  $\mathbf{x}(t_0)$  can be determined given measurements  $\mathbf{y}(t_k)$ . Therefore, solving for  $\mathbf{x}(t_0)$  results in:

$$\mathbf{x}(t_0) = (\mathbf{H}(t_k)^T \mathbf{H}(t_k))^{-1} \mathbf{H}(t_k)^T \mathbf{y}(t_k). \quad (10)$$

In the above equation,  $\mathbf{x}(t_0)$  can be determined if  $\mathbf{H}(t_k)^T \mathbf{H}(t_k)$  is invertible.  $\mathcal{O} = \mathbf{H}(t_k)^T \mathbf{H}(t_k)$  is called the observability matrix and has the following form:

$$\mathcal{O} = \sum_{k=1}^m \Phi(t_k, t_0)^T \tilde{\mathbf{H}}(t_k)^T \tilde{\mathbf{H}}(t_k) \Phi(t_k, t_0), \quad (11)$$

where  $m$  is the number of measurements. Similar derivations are found in: [2, 6, 10].

The criteria used for observability here is whether or not the observability matrix,  $\mathcal{O}$ , is invertible. The invertibility of a matrix can be determined by checking the matrix rank. The rank of a matrix can be determined by checking whether the eigenvalues or singular values are non-zero. Advantages of using singular values are that they are always positive and they can be computed for non-square matrices [17]. In order to determine the invertibility numerically in this work, the singular values of the observability matrix are computed. As introduced in [4], a tolerance must be implemented to determine when a value is numerically greater than zero. The tolerance is defined by:

$$Tol = \max(s_i) \times \max(\text{size}(\mathcal{O})) \times eps, \quad (12)$$

where  $s_i$  are the singular values of the observability matrix  $\mathcal{O}$  and  $eps$  is the machine precision or epsilon. This tolerance is one of many ways to represent the numerical error in a problem [12]. As more measurements get added to the observability matrix, the singular values will change.

This work specifically looks at extending the state vector beyond position and velocity, thus increasing the dimension of the observability matrix. In addition, measurement noise is incorporated using Cholesky decomposition and pre-whitening as in [4]. The measurement noise covariance is decomposed as follows:

$$\mathbf{K}^{-1} = \mathbf{L} \mathbf{L}^T. \quad (13)$$

Multiplying Equation 4 by the transpose of the lower triangular matrix,  $\mathbf{L}^T$ , a modified measurement equation has the form:

$$\mathbf{L}^T \mathbf{y}(t_k) = \mathbf{L}^T \mathbf{H}(t_k) \mathbf{x}(t_0). \quad (14)$$

The resulting observability matrix with measurement noise, following a similar process to Equations 9 and 10, is given by:

$$\mathcal{O} = \sum_{k=1}^n \Phi(t_k, t_0)^T \tilde{\mathbf{H}}(t_k)^T \mathbf{K}^{-1} \tilde{\mathbf{H}}(t_k) \Phi(t_k, t_0). \quad (15)$$

Next, the dynamical model used to compute the STM is introduced.

## 2.2. Dynamical Model

The state vector in this work is extended to include object characteristics which are parameters of solar radiation pressure (SRP): area-to-mass ratio (AMR),  $\frac{A}{m}$ , and the material dependent reflection coefficient,  $C$ . Therefore, the dynamics used in formulation of the STM and linearized measurement matrix must contain SRP perturbations. A simple cannonball model is used to derive the perturbing accelerations due to SRP, given by:

$$\mathbf{a}_{\text{SRP}} = -\frac{A}{m} C (\text{AU})^2 \frac{E}{c} \frac{\mathbf{s}}{|\mathbf{s}|^3}, \quad (16)$$

where  $C = \frac{1}{4} + \frac{1}{9} C_d$ ,  $C_d$  is the diffuse coefficient, AU is the astronomical unit,  $E = 1367.0 \text{ W/m}^2$  is the solar constant,  $c = 2.998 \times 10^8 \text{ m/s}$  is the speed of light, and  $\mathbf{s} = \mathbf{r}_{\text{sun}} - \mathbf{r}_{\text{obj}}$  is the sun-object vector, which is the distance from the sun to the object. The position vector of the sun to the center of the Earth is given by  $\mathbf{r}_{\text{sun}}$ , and the position vector of the object from the center of the Earth is given by  $\mathbf{r}_{\text{obj}}$ . Similar forms of the SRP perturbing acceleration can be found in: [8, 16]. Once methods for extending the observability state vector have been developed, higher-fidelity SRP models can be implemented, e.g., a flat plate model and modeling of Earth's shadow.

The equations of motion using the simple two body problem and SRP are given by:

$$\ddot{\mathbf{r}} = -\frac{\mu}{|\mathbf{r}|^3} \mathbf{r} + \mathbf{a}_{\text{SRP}}, \quad (17)$$

where  $\mathbf{r}$  is the position vector of the object and  $\mu = 3.986 \times 10^{14} \text{ m}^3/\text{s}^2$  is the standard gravitational parameter of Earth. Using the methods in Montenbruck [8], the  $\mathbf{A}(t_k)$  matrix in the STM differential equation for a state extended with AMR is given by:

$$\mathbf{A}(t_k) = \begin{bmatrix} \mathbf{0}_{3 \times 3} & \mathbf{I}_{3 \times 3} & \mathbf{0}_{3 \times 1} \\ \mathbf{G}_{\text{tot}}(t_k) & \mathbf{0}_{3 \times 3} & \frac{\partial \mathbf{a}_{\text{SRP}}(t_k)}{\partial \mathbf{x}(7)} \\ \mathbf{0}_{1 \times 3} & \mathbf{0}_{1 \times 3} & \mathbf{0}_{1 \times 1} \end{bmatrix}, \quad (18)$$

where  $\mathbf{G}_{\text{tot}}(t_k) = \mathbf{G}_{\text{grav}} + \mathbf{G}_{\text{SRP}}$  is the sum of the Jacobians of the equations of motion, when reduced to six first order differential equations. The partial derivatives of the extra state element beyond position and velocity, e.g. AMR or  $C$ , are given by  $\frac{\partial \mathbf{a}_{\text{SRP}}(t_k)}{\partial \mathbf{x}(7)}$ . The Jacobian of

the accelerations due to the central body with respect to the position components,  $\mathbf{G}_{\text{grav}}$ , is given by [8]:

$$\mathbf{G}_{\text{grav}} = \frac{\mu}{|\mathbf{r}|^5} \left( 3 \mathbf{r} \mathbf{r}^T - |\mathbf{r}|^2 \mathbf{I}_{3 \times 3} \right). \quad (19)$$

Next, the Jacobian of the SRP perturbing acceleration with respect to the position components has a similar form:

$$\mathbf{G}_{\text{SRP}} = -\frac{A}{m} C (\text{AU})^2 \frac{E}{c} \frac{1}{|\mathbf{s}|^5} \left( 3 \mathbf{s} \mathbf{s}^T - |\mathbf{s}|^2 \mathbf{I}_{3 \times 3} \right). \quad (20)$$

In this work, three different state extensions are tested: AMR, (AMR· $C$ ), and AMR &  $C$ . The first case extends the state vector by one variable, area-to-mass ratio. The second case extends the state by one variable, the product of AMR and  $C$ . The third case extends the state by two variables, AMR and  $C$ , separately. The partial derivatives for the first and second cases are given by:

$$\frac{\partial \mathbf{a}_{\text{SRP}}(t_k)}{\partial \text{AMR}} = \frac{\mathbf{a}_{\text{SRP}}(t_k)}{\text{AMR}} \quad (21)$$

$$\frac{\partial \mathbf{a}_{\text{SRP}}(t_k)}{\partial (\text{AMR} \cdot C)} = \frac{\mathbf{a}_{\text{SRP}}(t_k)}{(\text{AMR} \cdot C)} \quad (22)$$

Since the third state extension case adds two variables to the state,  $\mathbf{A}(t_k)$  is now size  $8 \times 8$  rather than  $7 \times 7$ , when only one state variable was added to the position and velocity state vector. The  $\mathbf{A}(t_k)$  for the third state extension case is given by:

$$\mathbf{A}(t_k) = \begin{bmatrix} \mathbf{0}_{3 \times 3} & \mathbf{I}_{3 \times 3} & \mathbf{0}_{3 \times 1} & \mathbf{0}_{3 \times 1} \\ \mathbf{G}_{\text{tot}}(t_k) & \mathbf{0}_{3 \times 3} & \frac{\partial \mathbf{a}_{\text{SRP}}(t_k)}{\partial \text{AMR}} & \frac{\partial \mathbf{a}_{\text{SRP}}(t_k)}{\partial C} \\ \mathbf{0}_{2 \times 3} & \mathbf{0}_{2 \times 3} & \mathbf{0}_{2 \times 1} & \mathbf{0}_{2 \times 1} \end{bmatrix}, \quad (23)$$

where,

$$\frac{\partial \mathbf{a}_{\text{SRP}}(t_k)}{\partial C} = \frac{\mathbf{a}_{\text{SRP}}(t_k)}{C}. \quad (24)$$

For each state extension case, the  $\mathbf{A}(t_k)$  is used to numerically determine the STM by solving Equation 6. Next, the linearized measurement matrix is formed.

## 2.3. Measurement Model

The next component of the observability matrix is the linearized measurement matrix,  $\tilde{\mathbf{H}}(t_k)$ , which is given by:

$$\tilde{\mathbf{H}}(t_k) = \frac{\partial \mathbf{y}(t_k)}{\partial \mathbf{x}(t_k)}, \quad (25)$$

where  $\mathbf{y}$  are the measurements right ascension,  $\alpha$ , declination,  $\delta$ , right ascension rate,  $\dot{\alpha}$ , and declination rate,  $\dot{\delta}$  at each time  $t_k$ . The measurements, for a topocentric observer located with latitude,  $\phi$ , and sidereal time,  $\theta$ , are

given by:

$$\alpha = \arctan\left(\frac{\bar{y}}{\bar{x}}\right), \quad (26)$$

$$\delta = \arctan\left(\frac{\bar{z}}{\sqrt{\bar{x}^2 + \bar{y}^2}}\right), \quad (27)$$

$$\dot{\alpha} = \frac{\bar{x}\dot{\bar{y}} - \bar{y}\dot{\bar{x}}}{\bar{x}^2 + \bar{y}^2}, \quad (28)$$

$$\dot{\delta} = \frac{-\bar{z}(\bar{x}\dot{\bar{x}} + \bar{y}\dot{\bar{y}}) + (\bar{x}^2 + \bar{y}^2)\dot{\bar{z}}}{\sqrt{\bar{x}^2 + \bar{y}^2}(\bar{x}^2 + \bar{y}^2 + \bar{z}^2)}, \quad (29)$$

where,

$$\bar{x} = x - R_{\oplus} \cos \phi \cos \theta, \quad (30)$$

$$\bar{y} = y - R_{\oplus} \cos \phi \sin \theta, \quad (31)$$

$$\bar{z} = z - R_{\oplus} \sin \phi, \quad (32)$$

$$\dot{\bar{x}} = \dot{x} + R_{\oplus} \dot{\theta} \cos \phi \sin \theta, \quad (33)$$

$$\dot{\bar{y}} = \dot{y} - R_{\oplus} \dot{\theta} \cos \phi \cos \theta. \quad (34)$$

$R_{\oplus}$  is the radius of the Earth and  $\dot{\theta}$  is the time rate of change of the sidereal time, which is the angular velocity of the Earth. The sidereal time is a function of the epoch and the observer longitude. The  $x, y, z, \dot{x}, \dot{y},$  and  $\dot{z}$  variables are Earth centered inertial position and velocity components. When the state is extended to include SRP parameters, the matrix defined by Equation 25, contains an extra column for each added state element. However, these columns are zero for the extended state cases given in Section 2.2, since the measurements,  $\mathbf{y} = [\alpha \ \delta \ \dot{\alpha} \ \dot{\delta}]^T$ , do not depend on AMR or  $C$ . The measurement noise has been defined using the works of Sanson and Frueh [13, 14] with specific values given in Section 3.

### 3. RESULTS

Five low Earth orbit (LEO) objects and five geosynchronous (GEO) objects were used to determine the effect of extending the state vector in observability analysis. The observer location used in this work is the ZIM-LAT telescope, Zimmerwald Observatory, Switzerland. The latitude and longitude of the telescope are  $46.8670^\circ$  and  $7.4670^\circ$ , respectively. The epoch used in this analysis is 53159.5 MJD. The four observability analysis cases simulated were for a non-extended state and three extended state cases. The three extended state cases are extending the state with AMR, (AMR  $\cdot$   $C$ ), and AMR &  $C_d$ . The first and second state extension cases extend the state by one variable, and the third case extends the state by two variables. The diffuse coefficient for all of the objects simulated is  $C_d = 0.5$ , leading to a  $C \approx 0.3056$ . Several of the GEO objects are HAMR objects with AMR values above the typical value for a GPS satellite  $0.02 \text{ m}^2/\text{kg}$ .

Also, measurement noise is incorporated into the analysis to see the combined impact of extending the state vector and including measurement noise. Table 1 gives the different measurement noise cases tested. Observability

analysis with each of the extended state cases was performed without measurement noise, with a noise ratio of 1.0, and with a noise ratio of 0.25. The noise ratio is defined by the ratio between the angle measurements and the ratio between the angular rate measurements.

$$\text{Noise ratio} = \frac{\sigma_{\alpha}^2}{\sigma_{\delta}^2} = \frac{\sigma_{\dot{\alpha}}^2}{\sigma_{\dot{\delta}}^2} \quad (35)$$

The ten orbit cases tested are given in Tables 2 and 3. GEO 1, GEO 3, and GEO 5 in Table 2 are high-area-to-mass ratio (HAMR) objects.

Table 1. Measurement Noise Cases.

Noise Ratio Case	Value
No Noise	-
Ratio = 1.0	$\sigma_{\alpha}^2 = \sigma_{\delta}^2 = 1.0 \text{ arcsec}$ $\sigma_{\dot{\alpha}}^2 = \sigma_{\dot{\delta}}^2 = 20.0 \text{ arcsec/sec}$
Ratio = 0.25	$\sigma_{\alpha}^2 = 1.0 \text{ arcsec}, \sigma_{\delta}^2 = 4.0 \text{ arcsec}$ $\sigma_{\dot{\alpha}}^2 = 20.0 \text{ arcsec/sec},$ $\sigma_{\dot{\delta}}^2 = 80.0 \text{ arcsec/sec}$

#### 3.1. GEO Extended State Observability

The invertibility of the observability matrix, Equation 11, is determined at each time step  $t_k$ . The matrix is invertible when the singular values are all greater than zero. Since this is being numerically determined, a tolerance, given by Equation 12, is implemented to account for numerical errors in the analysis. Therefore, for each of the extended state and measurement noise observability cases presented, the singular values of the observability matrix are compared to the tolerance.

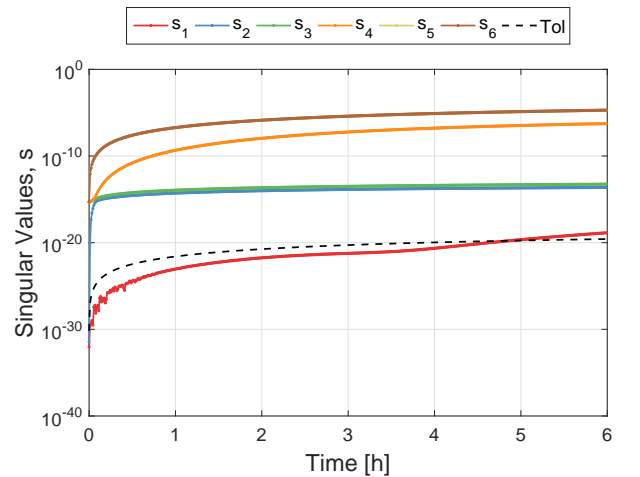


Figure 1. GEO 4 baseline observability case with only position and velocity in the state vector, where  $s_i$  denotes the singular values of the observability matrix.

Table 2. GEO Test Orbits

Orbit #	1	2	3	4	5
a (km)	42170.238	42190.793	42164.796	42166.668	42308.743
e (-)	9.7343e-4	4.9220e-4	1.5716e-3	1.6556e-4	3.1852e-4
i (deg)	35.7448	2.6447	7.4310	0.051497	13.8121
$\Omega$ (deg)	359.3036	295.4140	52.7661	123.2611	30.9790
$\omega$ (deg)	124.1101	255.2388	114.5845	79.7058	346.1611
$\nu$ (deg)	0.0	0.0	0.0	0.0	0.0
AMR (m <sup>2</sup> /kg)	5.00	0.02	1.00	0.02	20.0

Table 3. LEO Test Orbits

Orbit #	1	2	3	4	5
a (km)	8124.9673	7464.0111	7059.5685	7868.6408	7011.9387
e (-)	1.4686e-1	1.1651e-2	1.3704e-2	2.2336e-3	1.7747e-3
i (deg)	32.8687	28.3284	65.0611	74.0150	39.7500
$\Omega$ (deg)	55.8261	302.1046	18.5642	107.5861	28.6732
$\omega$ (deg)	53.8800	183.3909	176.8673	260.0122	58.1497
$\nu$ (deg)	0.0	0.0	0.0	0.0	0.0
AMR (m <sup>2</sup> /kg)	0.02	0.02	0.02	0.02	0.02

Figure 1 shows the results of observability analysis for the GEO 4 object with a non-extended state vector, containing position and velocity only. This analysis is performed without measurement noise. Each of the six singular values of the observability matrix, given by the colored lines in Figure 1, correspond to the six state elements. The tolerance line, given by Equation 12, is shown as a black dashed line. When all of the singular values go above the tolerance line, the observability matrix is invertible, and therefore, the system is observable. The measurement spacing used in this case is measurements every 40.0 seconds. Given this measurement spacing and the initial conditions in Table 2, the position and velocity of this object become observable after approximately 4.867 hours. Since this GEO 4 orbit is close to circular and equatorial, the z-components of position and velocity are difficult to determine from measurements. This behavior can be seen in Figure 1, where the smallest singular value in red takes longer to cross the tolerance line than all of the other singular values. Note that in Figure 1, the fifth and sixth singular values, given in yellow and brown, respectively, are indistinguishable in the plot.

Next, the state vector is extended to include AMR. When the AMR is incorporated into the observability analysis, Equation 18 is used to form the STM, and the linearized measurement matrix has an extra column of zeros. Furthermore, the tolerance changes since the dimension of the observability matrix is now  $7 \times 7$ .

Figure 2 shows the extended state observability analysis results with AMR added to the state vector. Seven singular values are now compared to a tolerance line. With the

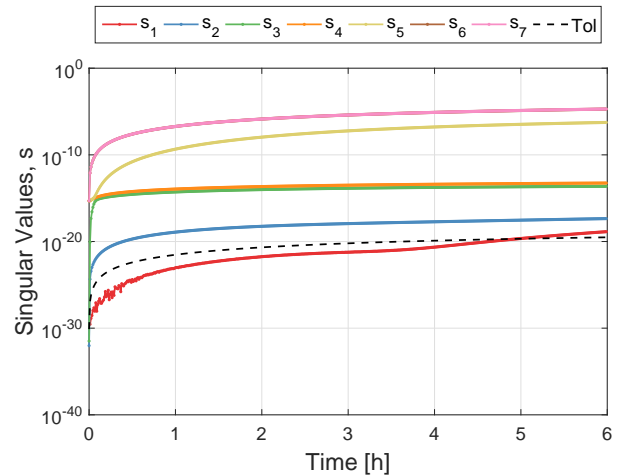


Figure 2. GEO 4 extended state observability with AMR, where  $s_i$  denotes the singular values of the observability matrix.

addition of AMR to the state, the smallest singular value crosses the tolerance line in approximately 4.956 hours, with observations every 40.0 seconds. Because of the addition of AMR to the state vector, more information must be determined from the measurements; therefore, more measurements, and thus more time, are required for the system to become observable.

The next extended state case tested considers the quantity (AMR  $\cdot$  C) together as one state element. When these two quantities are added to the state vector as one element to-

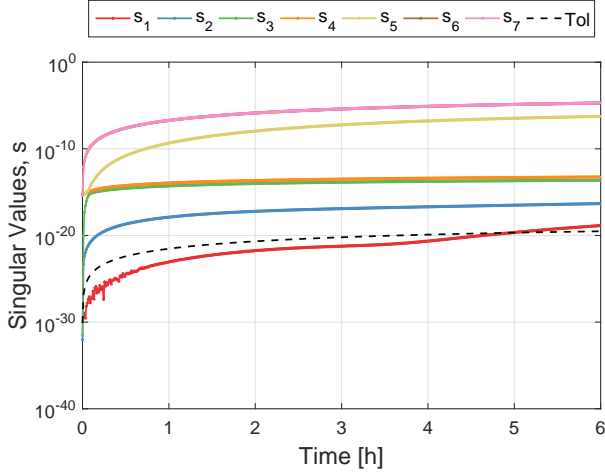


Figure 3. GEO 4 extended state observability with the quantity  $(AMR \cdot C)$ , where  $s_i$  denotes the singular values of the observability matrix.

gether, then the system does become observable, as seen in Figure 3. The time to become observable in this case with measurements every 40.0 seconds is approximately 4.956 hours, which is the same as the first extended state case. In this case of considering  $(AMR \cdot C)$  together, the observability analysis is determining the effect of a constant of the SRP perturbing acceleration on the time to become observable. For this object, the first and second extended state cases have the same time to become observable; this may not always be the case since the parameter added to extend the state is different: AMR versus  $(AMR \cdot C)$ , as seen in the LEO results of Section 3.2.

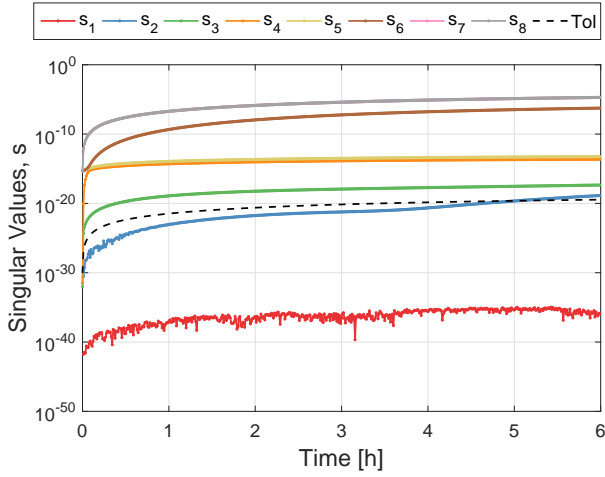


Figure 4. GEO 4 extended state observability with AMR and  $C$ , where  $s_i$  denotes the singular values of the observability matrix.

The final extended state case tested in this work, is the extension by two variables, AMR and  $C$ . In this case, the observability matrix uses a STM formed with Equation 23, which is dimension  $8 \times 8$ . When two constants used in the perturbing acceleration are added to the state vec-

tor in observability analysis, the system is not observable. This can be seen in Figure 4, where the smallest singular value in red does not cross the tolerance line. Even if this analysis were to be extended with more measurements and thus more time, this system would not become observable. Since AMR and  $C$  are both constants in the SRP perturbing acceleration, measurements of right ascension, declination, and the angular rates are not sufficient for determining changes in the orbit due to AMR compared to changes due to  $C$ . However, if different measurement types were added to this analysis, which could be used to determine AMR or  $C$ , then this system would become observable after some time.

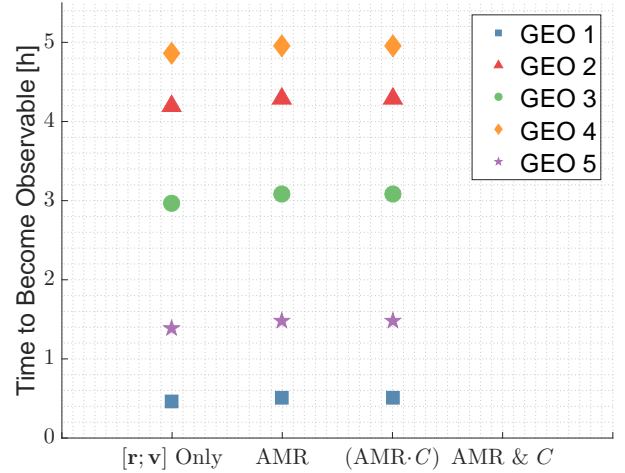


Figure 5. All five GEO objects without measurement noise.

The times to become observable for all five of the GEO objects without measurement noise for each of the extended state cases are given in Figure 5. The increase in each of the times to become observable as a result of extending the state can be seen. Also, note that the extended state case with AMR &  $C$  as separate state elements is unobservable for each GEO object. In addition, for these five GEO objects, the time to become observable is dependent on inclination of the orbit. A larger inclination, as in GEO 1, results in a lower time to become observable. Conversely, a smaller inclination, as in GEO 4, results in a longer time to become observable. The times for each object to become observable are given in Table 4.

Next, each of the extended state observability analysis cases for the five GEO objects are performed with measurement noise ratios given in Table 1. The observability matrix in this analysis includes measurement noise given by Equation 15. The times for the smallest singular value of each noise case to cross the tolerance line are shown in Figure 6. The times to become observable are on the y-axis in hours, and the different extended state cases are on the x-axis. The blue squares represent the cases without measurement noise. The red triangles and the green circles represent the two different measurement noise ratio cases. In all of the noise cases tested, the impact of extending the state is given by the increase in the time to

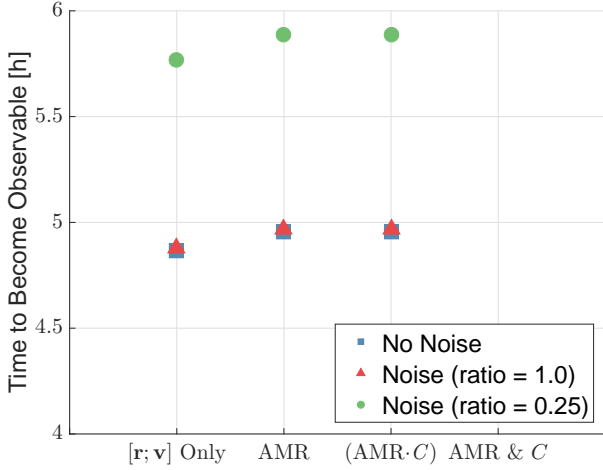


Figure 6. GEO 4 extended state observability cases with measurement noise.

become observable.

The changes in the times to become observable resulting from the measurement noise are explained in previous work on incorporating measurement noise into observability analysis [4]. For the GEO 4 object, which is nearly circular and equatorial, the declination measurements are important for determining the z-components of the state. Therefore, when the noise in the declination measurements is four times larger than the measurement noise in right ascension, noise ratio = 0.25, the time to become observable increases. In addition, the previous results of incorporating measurement noise into observability analysis showed that when the noise ratio equals one there is only a small change in the time to become observable, which is also seen in Figure 6. Next, similar results are presented for the five LEO objects.

### 3.2. LEO Extended State Observability

Similar trends to the GEO extended state observability results can be seen in the LEO extended state observability results. The five LEO objects simulated are given in Table 3. The times to become observable for the LEO objects are shorter than the times for the GEO objects because of the higher orbit energy of the LEO objects; the states of the LEO objects change by a larger amount than the states of the GEO objects in the same amount of time. The extended state observability results without measurement noise for the LEO objects are summarized in Figure 7.

For each LEO object in Figure 7, the time to become observable increases when an extra state element is added to the analysis, with changes of several orders of magnitude for a few of the objects. The perturbing effect of SRP on a LEO object is much smaller than on a GEO object. Therefore, these large changes in the time to become observable are explained by how much of an effect SRP has on the LEO objects. Since the SRP perturbation effect on

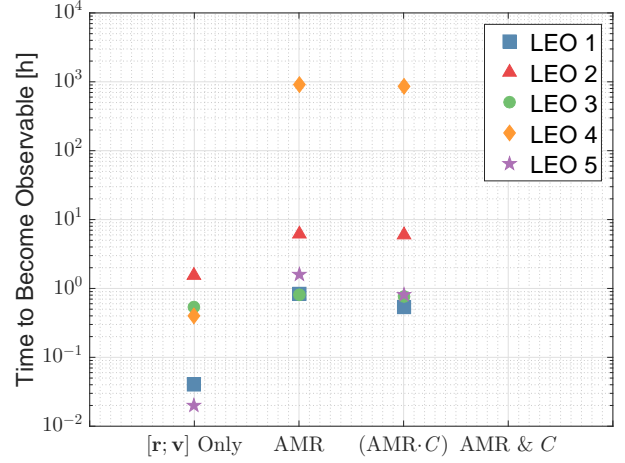


Figure 7. All five LEO objects without measurement noise.

LEO objects is small relative to other perturbing forces, the time for the extended state parameters to become observable increases. Unlike the GEO results, there is not a clear dependence on inclination for the LEO objects. The location of the observer becomes more significant for the LEO objects, so dependence on inclination is not as clear. Another interesting result for the LEO observability analysis is the decrease in the time to become observable from the extended state case with AMR to the extended state case with (AMR·C). This result is seen more clearly in Figure 8.

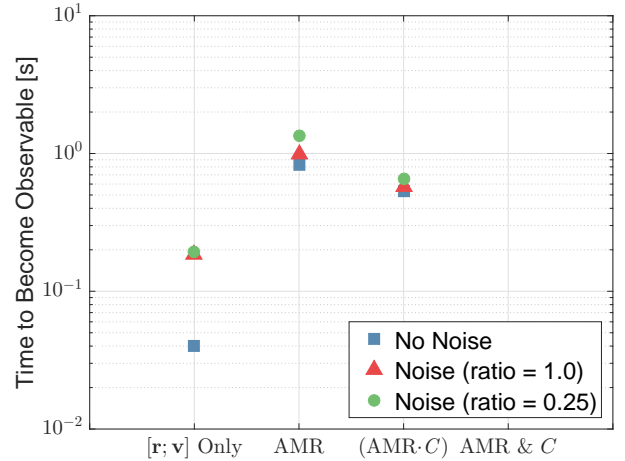


Figure 8. LEO 1 extended state observability cases with measurement noise.

The  $\mathbf{A}(t_k)$  matrix used to define the STM at each time step will be different for the two cases. The last column of the  $\mathbf{A}(t_k)$  contains the term  $\frac{\partial \mathbf{a}_{\text{SRP}}(t_k)}{\partial \mathbf{x}(7)}$ . When  $\mathbf{x}(7)$  is the combined term (AMR·C), the three terms in the last column of  $\mathbf{A}(t_k)$  are smaller values or more negative because  $C \approx 0.3056$ . These smaller values in the  $\mathbf{A}(t_k)$  matrix result in a larger value of the smallest singular value of the observability matrix. A rigorous proof of this behavior is yet to be determined, but this behavior

accounts for the decrease in the time to become observable when extending the state with the combined term (AMR·C) compared to extending the state with AMR only. In Figure 7, it appears that only some objects exhibit this behavior of decreased time to become observable between the two extended state cases, but the times given in Table 5 show that the times to become observable in the combined extend state case are less than the times to become observable than the AMR only extended state case. This behavior is not seen with the five GEO objects tested; this could be due to the differences in the effect of SRP on LEO and GEO objects, or it could also be due to the large time steps used in the GEO analysis.

Figure 8 also depicts the impact of measurement noise on the time to become observable. Similar to the findings of previous work on measurement noise in observability analysis, for the LEO 1 object, greater measurement noise on either of the measurements than the other will increase the time to become observable [4]. Furthermore, even the noise case where the noise ratio is one is not necessarily the shortest time to become observable. In addition, the analysis performed in previous work on this topic looked at angles-only measurements, so these results are not exactly comparable, but some similar trends are apparent.

### 3.3. Times To Become Observable

Tables 4 and 5 summarize the times to become observable for each of the extended state cases without measurement noise. The GEO times are given in hours and the LEO times are given in seconds. In Section 3.2 and specifically, Figure 7, an interesting behavior was seen with several of the times to become observable being lower for the combined (AMR·C) extended state case compared to the AMR extended state case. Even though the behavior is not apparent for all of the LEO objects, Table 5 shows that the times to become observable for the (AMR·C) case are less than the AMR case. This trend is due to the size of the  $\frac{\partial \mathbf{a}_{SRP}(t_k)}{\partial \mathbf{x}(7)}$  terms in the formulation of the STM. A similar behavior is suspected for the GEO objects, but the larger time steps may be obscuring the differences in the times to become observable between the two extended state cases.

Table 4. Times to become observable for the GEO objects with extended states and without measurement noise, times given in hours.

Orbit #	[r; v]	AMR	(AMR·C)	AMR & C
1	0.467	0.511	0.511	–
2	4.2	4.289	4.289	–
3	2.967	3.078	3.078	–
4	4.867	4.956	4.956	–
5	1.389	1.478	1.478	–

Next, Table 6 gives the same times to become observable

Table 5. Times to become observable for the LEO objects with extended states and without measurement noise, times given in seconds.

Orbit #	[r; v]	AMR	(AMR·C)	AMR & C
1	0.04	0.824	0.536	–
2	1.552	6.08	5.92	–
3	0.536	0.808	0.768	–
4	0.40	904.0	864.0	–
5	0.02	1.60	0.80	–

as Table 4, but with the time the seventh singular value of the AMR & C extended state case crosses the tolerance line. For all of the GEO objects, the time for this seventh singular value of the AMR & C extended state case to cross the tolerance line is greater than the times to become observable for the AMR and (AMR·C) cases. Therefore, this indicates that the times to become observable for seven of the state parameters increases when an eighth parameter of the state is unobservable.

Table 6. Seventh singular values of the AMR & C extended state case for the GEO objects.

Orbit #	[r; v]	AMR	(AMR·C)	AMR & C (7th s)
1	0.467	0.511	0.511	0.544
2	4.2	4.289	4.289	4.367
3	2.967	3.078	3.078	3.178
4	4.867	4.956	4.956	5.044
5	1.389	1.478	1.478	1.567

All of the LEO objects for the AMR & C extended state, given in Table 7, exhibit the same trend as found in Table 6, where the time for the second smallest singular value of the AMR & C extended state case to go above the tolerance line is greater than the times for the other extended state cases to become observable.

Table 7. Seventh singular values of the AMR & C extended state case for the LEO objects.

Orbit #	[r; v]	AMR	(AMR·C)	AMR & C (7th s)
1	0.04	0.824	0.536	0.856
2	1.552	6.08	5.92	8.56
3	0.536	0.808	0.768	0.832
4	0.40	904.0	864.0	1052.0
5	0.02	1.60	0.80	1.672

### 3.4. Observations Spacing for Sensor Tasking

Next, more realistic observation spacing is implemented in the discrete-time observability analysis. In addition, propagation time is extended to determine whether there is a point at which the singular values are at a maximum over an orbit.

The following results are for discrete-time observability analyses, where observations are taken in three batches, with five observations per batch and 100 seconds between each observation. The time between the observations batches is varied to determine if there is a point where the information from the observations is maximized. Intuitively, and from initial orbit determination methods, spreading observations farther apart should provide more information about an orbit. However, the geometry of the orbit and observer complicates how observations should be spaced to maximize observability.

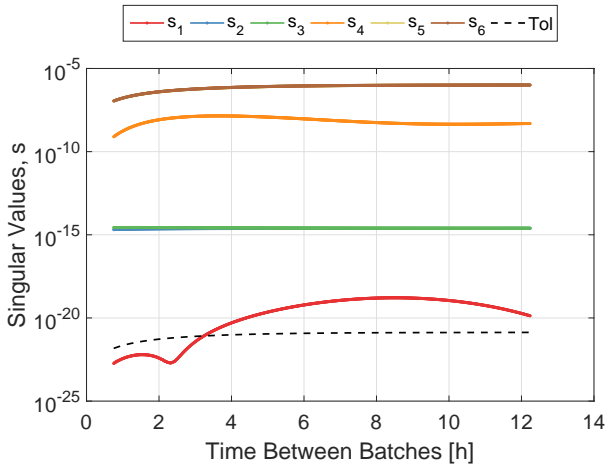


Figure 9. GEO 4  $[\mathbf{r}; \mathbf{v}]$  observability with three batches of observations, where  $s_i$  denotes the singular values of the observability matrix.

Figure 9 shows the singular values of the observability matrix for the GEO 4 object with only  $\mathbf{r}$  and  $\mathbf{v}$  in the state vector. The y-axis contains the six singular values of the observability matrix corresponding to the six state elements, and the x-axis is the spacing between observation batches. For example, at the eight hour spacing mark, batches of observations would be taken at  $t = 0.0$  h,  $t = 8.0$  h (0.334 period), and  $t = 16.0$  h (0.668 period). Note that the system becomes observable when three batches of observations are spread by approximately 3.24 hours. Changing the number of observation batches and the number of observations per batch will change the spacing between batches required for the system to become observable. In addition to the point where this system becomes observable, another point of interest is where the smallest singular value, given in red in Figure 9, is at a maximum. When this point is at a maximum, given it is above the tolerance line, this point could be considered as the best time to observe the object. In the presence of measurement noise and uncertainty in the state used to calculate the STM and linearized measurement

matrix, the singular value curve given in red may change slightly; therefore, the best time to observe this object to ensure observability of the state elements is to space the observation batches so the singular values will be furthest from the tolerance line. For Figure 9, this point occurs when observations batches are spread by approximately 8.49 hours.

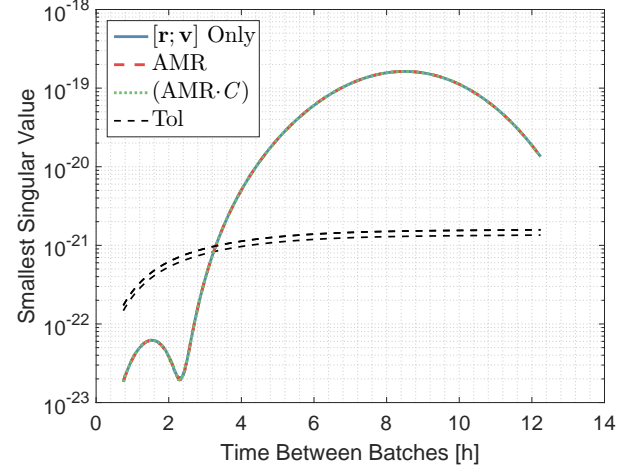


Figure 10. Smallest singular values of the different GEO 4 observability cases with three batches of observations.

Next, the same simulations were performed for two of the extended state cases: AMR and  $(\text{AMR} \cdot C)$ . Figure 10 shows the smallest singular value of each observability run against the spacing between observation batches. Note there are two tolerance lines because the extended state analysis has an observability matrix of dimension seven rather than dimension six of the observability matrix for the analysis with position and velocity only. On the scales given, the points where these curves cross the tolerance lines appears to be the same, but upon closer inspection the crossing points are slightly different.

The addition of the SRP parameters in the state was expected to change the best time to observe an object, similar to how the time to become observable, in Table 4, changed with addition of the extra state parameter. However, the point of maximum observability did not change for the GEO 4 object; the maximum point of each observability run in Figure 10 is the same, approximately 8.49 hours. Differences in the maximum point could be obscured by the time step used in this analysis, 40.0 seconds. However, the reason for performing this analysis of finding the maximum point is to determine whether or not extending the state will drastically change this maximum point; therefore, changes smaller than the time step of 40.0 seconds would not be significant.

This analysis is repeated for the GEO 1 object which has a larger  $\text{AMR} = 5.0 \text{ m}^2/\text{kg}$ . Figure 11 shows the observability analysis results for the GEO 1 object with changing the spacing between observation batches. The smallest singular value curve, given in red, has a different shape than the corresponding GEO 4 curve.

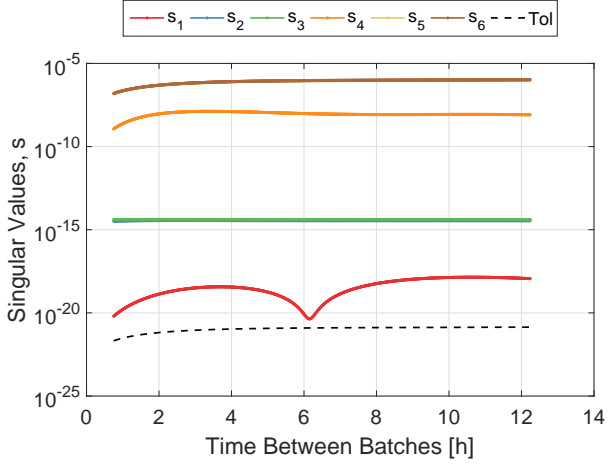


Figure 11. GEO 1  $[\mathbf{r}; \mathbf{v}]$  observability with three batches of observations, where  $s_i$  denotes the singular values of the observability matrix.

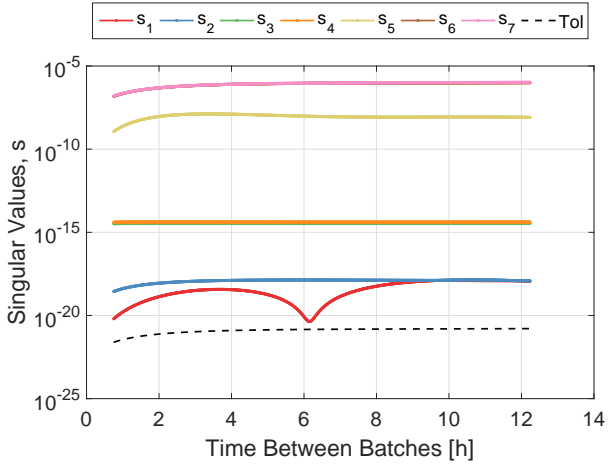


Figure 12. GEO 1 AMR extended state observability with three batches of observations, where  $s_i$  denotes the singular values of the observability matrix.

Figure 12 shows the observability analysis results for the GEO 1 object with a state extended by AMR. The smallest singular value curve appears to be bounded by the second smallest singular value. The red curve never actually is the same as the blue curve in Figure 12, but it does change the shape of the red curve when compared to the results for only position and velocity in the state. The smallest singular value curves for the different extended state cases are compared in Figure 13.

In Figure 13, the smallest singular value curves match except for the region where observation batches are spaced between approximately 9.5 and 12.0 hours. However, the value of the maximum for the blue and green curves is close to the value of the red curve at the same observation spacing. Therefore, the differences in the singular value curves will not affect the maximum observability point significantly.

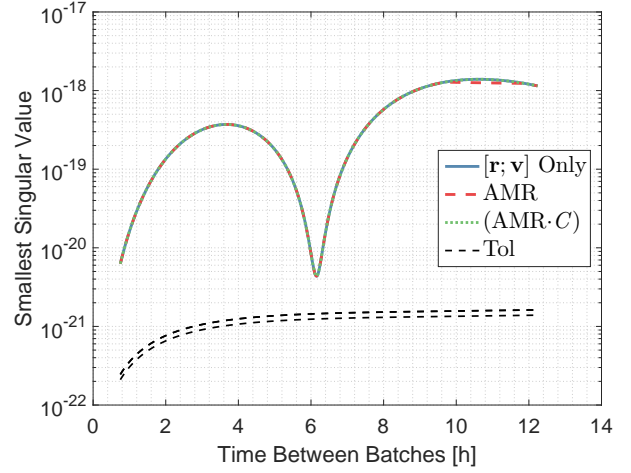


Figure 13. Smallest singular values of the different GEO 1 observability cases with three batches of observations.

#### 4. CONCLUSIONS AND FUTURE WORK

This work focused on the implementation and effects of extending the state vector in observability analysis. Discrete-time observability methods use an observability matrix formed with the state transition matrix (STM) and the linearized measurement matrix. This analysis was extended beyond the position and velocity state by including parameters of solar radiation pressure (SRP): area-to-mass ratio (AMR) and the material dependent reflection coefficient,  $C$ . In order to incorporate these parameters in the observability analysis, the SRP perturbing acceleration is included with the two body dynamics. Therefore, the Jacobian of the SRP acceleration with respect to the state is used in the formulation of the STM differential equation. Also, when SRP parameters are added to the extended state, extra columns are added to the linearized measurement matrix.

Discrete time-varying observability analysis was performed for ten objects, five low Earth orbit (LEO) objects and five geosynchronous (GEO) objects. Each of the ten objects were simulated for four different cases: position and velocity only and three extended state cases. The three extended state cases were AMR,  $(AMR \cdot C)$ , and AMR &  $C$ , where  $C = \frac{1}{4} + \frac{1}{9}C_d$ . Furthermore, measurement noise is added to the observability analysis to see the combined effect of extending the state and measurement noise.

The system is considered observable when the smallest singular value of the observability matrix is greater than a tolerance line defined by the largest singular values, size of the observability matrix, and the machine epsilon. The effects of extending the state vector in the observability analysis can be seen in the times to become observable. The times to become observable increased when solar radiation pressure parameters were added to the position and velocity state. Furthermore, one of the extended state cases, where AMR &  $C$  are considered as separate pa-

rameters, does not become observable for the angle and angular rate measurements used in this analysis. If different measurement types were to be added, the effect of AMR could be differentiated from the effect of  $C$ , thus making this case observable after some time. Even though this extended state case did not become observable in this analysis, the times for the second smallest singular value to become greater than the tolerance increased. Therefore, extending the state beyond what can become observable is detrimental to the other observable values in the system.

If specific object characteristics are desired, similar analyses to the methods implemented in this work could be implemented to determine what object characteristics are observable with specific measurement types and over specific time periods. If an object characteristic is included in the analysis and the characteristic is not observable, the rest of the system could be impacted as seen by the time to become observable in this work.

In addition, more realistic observation spacing was implemented, and the observability results looking at the time to become observable were extended to determine when the smallest singular value of the observability matrix was maximized. This maximum point of the smallest singular value could be considered as the observation time where the system is most observable.

Future work on extended state observability will focus on including different measurement types to resolve the AMR and  $C$  SRP parameters. Furthermore, work on the observation spacing will focus on determining the different trends seen in the GEO objects and why the differences in the extended state cases are occurring. In addition, realistic constraints will be placed on the times to observe an object and the measurement noise will be defined for specific sensor systems.

## ACKNOWLEDGMENTS

This material is based on research sponsored by Air Force Office of Scientific Research under agreement number FA9550-14-1-0348DEF. The author would also like to acknowledge the Indiana Space Grant Consortium for their support of this research.

## REFERENCES

1. Battin R., (1999). *An Introduction to the Mathematics and Methods of Astrodynamics*, American Institute of Aeronautics and Astronautics, Inc., Reston, Virginia, USA, Rev. ed..
2. Bay, J., (1999). *Fundamentals of Linear State Space Systems*, WCB/McGraw-Hill.
3. Dianetti, A., Weisman, R., and Crassidis, J., (2017). *Application of Observability Analysis to Space Object Tracking*, AIAA 2017-1258, AIAA SciTech Forum -

- AIAA Guidance, Navigation, and Control Conference, Grapevine, Texas, USA, January.
4. Friedman A., Frueh C., (2017). Observability analysis applied to artificial near-earth objects with noise. 27th AAS/AIAA Space Flight Mechanics Meeting, San Antonio, Texas, USA, February 5-9.
5. Frueh, C., (2015). *Observability of Non-cooperative Space Object's Tracking and Characterization*, 25th International Symposium on Space Flight Dynamics ISSFD, Munich, Germany, October.
6. Gajic, Z. and Lelic, M., (1996). *Modern Control Systems Engineering*, Prentice-Hall.
7. Leushacke D., Flury W., Jehn R., Klinkrad H., Landgraf M., (2002). *Detecting, Tracking and Imaging Space Debris*, ESA bulletin 109, February.
8. Montenbruck O., Gill E., (2012). *Satellite Orbits: Models, Methods, and Applications*, Springer-Verlag, Berlin, Heidelberg, Rev. ed..
9. NASA, (2015). *2015 NASA Technology Roadmaps: Introduction, Crosscutting Technologies, and Index*, National Aeronautics and Space Administration.
10. Ogata, K., (1967). *State Space Analysis of Control Systems*, Prentice-Hall, Inc., Englewood Cliffs, NJ.
11. Pelton J., (2016). *Tracking of Orbital Debris and Avoidance of Satellite Collisions*, Handbook of Satellite Applications, Springer, New York, pages 1-13.
12. Press W. H., Teukolsky S. A., Vetterling W. T, Flannery B. P., (2007). *Numerical Recipes*, Cambridge University Press, 3rd ed., page 795.
13. Sanson, F. and Frueh, C., (2017). Noise estimation and probability of detection in non-resolved images: application to space object observation, *Journal of Astronautical Science*, Submitted.
14. Sanson, F. and Frueh, C., (2017). Space Object Position Uncertainty Quantification in Non-Resolved Images, *IEEE Transactions of Signal Processing*, Submitted.
15. Tapley B., Schutz B., Born G., (2004). *Statistical Orbit Determination*, Elsevier Academic Press, Burlington, MA, USA.
16. Vallado D., (2001). *Fundamentals of Astrodynamics and Applications*, Microcosm Press, El Segundo, California, USA, Kluwer Academic Publishers, Boston, MA, USA, ed. 2.
17. Wilkinson, J., (1965). *The Algebraic Eigenvalue Problem*, Clarendon Press, Oxford University Press, Amen House, London.